

Tuning magnetic spirals beyond room temperature with chemical disorder

Mickaël Morin¹, Emmanuel Canévet², Adrien Raynaud¹, Marek Bartkowiak¹,
Denis Sheptyakov², Voraksmy Ban³, Michel Kenzelmann¹, Ekaterina
Pomjakushina¹, Kazimierz Conder¹ and Marisa Medarde^{1,*}

¹ Laboratory for Scientific Developments and Novel Materials,
Paul Scherrer Institut, CH-5232 Villigen PSI, Switzerland

² Laboratory for Neutron Scattering and Imaging,
Paul Scherrer Institut, CH-5232 Villigen PSI, Switzerland

³ Swiss Light Source,
Paul Scherrer Institut, CH-5232 Villigen PSI, Switzerland,

* Corresponding author (marisa.medarde@psi.ch)

In the past years, magnetism-driven ferroelectricity and gigantic magnetoelectric effects have been reported for a number of frustrated magnets featuring ordered spiral magnetic phases. Such materials are of high current interest due to their potential for spintronics and low-power magnetoelectric devices. However, their low magnetic ordering temperatures (typically $T_N < 100\text{K}$) greatly restrict their fields of application. Here we demonstrate that the onset temperature of the spiral phase in the perovskite YBaCuFeO_5 can be increased by more than 150K through a controlled manipulation of the Fe/Cu chemical disorder. Moreover we show that this novel mechanism can stabilize the magnetic spiral state of YBaCuFeO_5 above the symbolic value of 25°C at zero magnetic field. Our findings demonstrate that the properties of magnetic spirals, including its wavelength and stability range, can be engineered through the control of chemical disorder, offering a great potential for the design of materials with magnetoelectric properties beyond room temperature.

INTRODUCTION

Spiral magnetic order in non-geometrically frustrated transition metal oxides often arises from the competition between nearest-neighbor (NN) J and next-nearest-neighbor (NNN) J' superexchange interactions¹. As a true competition may only happen if the two contenders are of comparable strengths, J and J' should not be too different in magnitude. Yet in insulating transition-metal oxides NNN interactions are usually very weak². A direct consequence is that magnetic spirals usually appear in presence of small NN couplings, leading naturally to low order temperatures. There are very few examples of materials where both J and J' reach values large enough to stabilize spiral phases close to room temperature (RT). One of them is CuO, which combines a large J ³ with a J'/J ratio $\sim -1/5$ ⁴ close to the spiral stability criterion for a frustrated one-dimensional (1D) spin chain (Supplementary Fig.1)¹. A spiral phase is observed for temperatures above 200K, but only in a narrow temperature window of 17K⁵. Different strategies aimed to engineer the spiral stability range towards higher temperatures were proposed, but they turned out to be either unsuccessful⁶ or unpractical for applications⁷. In view of the high current interest on spiral magnets as potential for low-power magnetoelectric devices,⁸⁻²⁰ it is highly desirable to identify new mechanisms that yields high-temperature spiral phases in oxides.

To address this question we investigated the layered perovskite YBaCuFeO₅, one of the few oxides with a spin-spiral phase above 200K.^{5,20-21} As for CuO²², spontaneous electric polarization was reported to exist at zero magnetic field in the spiral phase,^{21,23-24} which is stable over a temperature range more than 10 times larger than in cupric oxide. Here we show that the Cu/Fe chemical disorder in YBaCuFeO₅ has a

tremendous impact on the degree of magnetic frustration, and that it can be used to tune the stability range of the spiral phase and to extend it beyond RT.

RESULTS

The crystal structure of YBaCuFeO_5 (space group $P4mm$), is shown in Fig.1a.²¹ It consists of two perovskite units where the A-site cations Ba^{2+} and Y^{3+} are ordered in layers. The B sites host Cu^{2+} and Fe^{3+} , but their tendency to order is less pronounced because of their similar ionic size. 1/6 of ordered O vacancies reduce the coordination of the B-site from octahedral to square-pyramidal, and as a result the BO_5 units, which are connected by the apexes, form layers of “bow ties” stacked along the **c** axis.

YBaCuFeO_5 undergoes two magnetic transitions at temperatures T_{N1} and T_{N2} .^{21,23-28} The high temperature collinear antiferromagnetic (AFM) phase ($T_{N1} > T > T_{N2}$) is characterized by the propagation vector $\mathbf{k}_c = (\frac{1}{2} \frac{1}{2} \frac{1}{2})$ (Fig.1b). In the **ab**-plane all possible NN J_{ab} interactions (Cu-Cu, Cu-Fe and Fe-Fe) are AFM and very strong (up to 130 meV), whereas weaker, up to 2 orders of magnitude smaller AFM (J_{c1}) and ferromagnetic (FM) J_{c2} couplings alternate along the **c** axis.²¹ The only FM coupling in the structure corresponds to ions occupying the bow-ties (J_{c2} , Fig.1a), and, according to the Goodenough-Kanamori-Anderson rules²⁹⁻³¹, this is only possible if they are occupied by Cu/Fe pairs. Since Cu and Fe are usually disordered in this material, this implies that the bow-ties are preferentially occupied by FM Cu-Fe “dimers” randomly distributed in the structure. The lower ground state energy of Fe-Cu distributions containing disordered FM Cu-Fe dimers has been confirmed by DFT calculations²¹.

Below T_{N2} the magnetic order becomes incommensurate along the \mathbf{c} axis and the neutron powder diffraction data are consistent with the appearance of an inclined circular helix with propagation vector $\mathbf{k}_i = (\frac{1}{2} \frac{1}{2} \frac{1}{2} \pm q)^{21}$. Interestingly, the deviation from collinearity in the spiral state occurs exclusively within the bow-ties, which lose their FM alignment below T_{N2} (Fig.1c). This suggests that J_{c2} is the magnetic coupling most sensitive to the thermal variation of the crystal structure. Other external perturbations such as high pressure, isovalent A-site substitutions or variations in the Fe/Cu distribution can thus be expected to affect it also significantly. To check this hypothesis we prepared five YBaCuFeO₅ ceramic samples using identical conditions apart from the cooling speed after the last annealing, which was systematically varied in order to obtain distinct degrees of Cu/Fe disorder (see Methods).

Fig.1d shows the magnetic susceptibility M/H of the five samples, where the two magnetic anomalies T_{N1} and T_{N2} are clearly visible. While T_{N1} decreases slightly with increasing cooling rates, T_{N2} displays the opposite behavior and undergoes a huge increase of more than 150K, reaching $T_{N2} = 310\text{K}$ for the sample with the fastest cooling rate. The appearance of Bragg reflections corresponding to $\mathbf{k}_c = (\frac{1}{2} \frac{1}{2} \frac{1}{2})$ below T_{N1} in the neutron diffraction patterns (Fig. 1e) confirms that this transition corresponds to the onset of the collinear AFM order. Below T_{N2} the magnetic reflections are progressively replaced by new incommensurate satellites corresponding to $\mathbf{k}_i = (\frac{1}{2} \frac{1}{2} \frac{1}{2} \pm q)$, characteristic of the magnetic spiral state (Supplementary Fig. 1). The temperature dependence of the magnetic modulation vector q is shown in Fig. 2a for the five samples and the ground state value (q_G) is

shown in Fig. 2b as a function of cooling rate. The angle φ_G between the **ab** plane and the rotation plane of the spiral at 10K is also displayed in Fig. 2b. Interestingly, there is a clear correlation between the cooling rate, the collinear-to-spiral transition temperature T_{N2} and the ground state values of q (q_G) and φ (φ_G). This means that the three main properties of the spiral, namely, the stability range, the periodicity and the inclination of the rotation plane can be tuned in a controlled way by the choice of the synthesis protocol.

To get insight about the mechanism behind these large magnetic differences, we employed high resolution neutron and synchrotron x-ray powder diffraction (see Methods and Supplementary Fig. 2) to investigate the structural modifications induced by the different cooling rates. The possible role of oxygen non-stoichiometry was ruled out after determining the total O-content by thermogravimetric H₂-reduction, which was found to be in excellent agreement with the nominal chemical formula and with the results from the Rietveld analysis (see Methods). Fig. 3a shows the evolution of the RT lattice parameters relative to the values obtained for the sample with the slowest cooling rate. A small increase of **a** (+0.02%) and a decrease of **c** about 3 times larger (-0.06%) are observed for faster cooling speeds. This means that a tensile ($c/2a < 1$) tetragonal distortion results in a more robust spiral state which grows at the expense of the collinear phase. Figs. 3c-d show the thickness of the bipyramid block (d_2) and that of the layers separating the bipyramids along **c** (d_1). While d_1 undergoes only a modest increase (+0.005Å), the decrease in d_2 is twice larger (-0.01Å). The large shrinkage of d_1 is thus at the origin of the contraction of **c** that is observed for faster cooling rates.

Figs. 4a and b show the evolution of the average apical and basal distances for the FeO_5 and CuO_5 pyramids. As expected from its Jahn-Teller electronic configuration ($t_{2g}^6 e_g^3$), the coordination polyhedron of Cu^{2+} is strongly distorted, with shorter in-plane distances and a much longer apical distance than Fe^{3+} ($t_{2g}^3 e_g^2$). Interestingly, none of the Fe-O/Cu-O distances change significantly with the cooling rate within the experimental error. This suggests that the contraction of the bow-ties may arise from a modification of the Cu/Fe distribution induced by different cooling speeds.

To check this scenario we examined the Cu/Fe occupation of the split B-sites. Their values, averaged over the whole sample volume, are shown in Figs. 4c-d and Supplementary Table 1 as function of the cooling rate. We note that the smallest difference between the Cu and Fe occupations (10%) is obtained for the quenched sample, where the Cu/Fe disorder promoted by the enhanced ionic diffusion at high temperatures is “frozen” by the fast cooling rate. Slower cooling results in a clear tendency towards a more ordered state reflected by a larger difference between the Cu/Fe occupations, which reaches 16% for the sample cooled at 5K h^{-1} . The large degree of Cu/Fe disorder in all samples is supported by the values of the mean-square displacements (MSD) at 10K. As shown in Figs. e-f and Supplementary Table 1, they are very small for Cu, Fe, Y and the basal oxygens, both in the **ab**-plane and along the **c**-axis, consistent with the reduced thermal motion expected at this temperature. For Ba and the apical oxygen, the MSD are also small in the **ab**-plane, but very large in the **c** direction, signaling a static contribution $\langle u_s^2 \rangle \sim 0.016\text{-}0.022 \text{ \AA}^2$ superimposed to the very weak thermal motion $\langle u_T^2 \rangle \sim 0.002\text{-}0.005 \text{ \AA}^2$. This reflects the length fluctuations of the apical distances in the bipyramids³²⁻³³, confirming the large degree of Cu/Fe disorder in *all* samples.

DISCUSSION

A remarkable observation is that very small differences in the average Cu/Fe disorder have a dramatic impact in the degree of magnetic frustration, resulting into a huge increase of the spiral stability range. A full understanding of this behavior needs additional information on the details of the Cu/Fe distribution that can be provided by techniques such as scanning microscopies, EXAFS or diffuse scattering. However, the observed evolution of d_1 and d_2 can already provide important hints about the expected impact of disorder on the couplings J_{c1} and J_{c2} . Looking to Figs. 1f, 3c, 3d and Supplementary Fig. 4 we note that T_{N1} and $1/d_1$ decrease for increasing cooling rates whereas T_{N2} and $1/d_2$ display the opposite behavior. It is thus tempting to associate the control of T_{N1} (and hence the appearance of 3D order) to inter-bipyramid coupling J_{c1} , and the setup of the spiral state at T_{N2} to the intra-bipyramid coupling J_{c2} . Also, given that the increase of T_{N2} with the cooling rate is much faster than the decrease of T_{N1} , the J_{c2} / J_{c1} ratio is probably a more appropriate control parameter.

The empirical relationship $T_{N2} \propto J_{c2} / J_{c1} \propto d_1 / d_2$ suggests that the spiral magnetic order in YBaCuFeO₅ could display some of the characteristics of a quasi-1D chain. However, the alternating AFM-FM-AFM-FM... chain along the **c** axis suggested by the collinear magnetic order (Fig. 1b) is not frustrated³⁴. As shown in ref.²¹, competition between NN (J_{c1} and J_{c2}) and NNN couplings along **c** could give rise to a spiral. However, the NNN couplings obtained by *ab initio* DFT calculations either are too small, or had the wrong sign²¹. The origin of the magnetic frustration in YBaCuFeO₅ remains thus mysterious, indicating that some important ingredient is still missing.

Since the degree of average Fe/Cu disorder plays a prominent role in the control of T_{N2} and q_G , disorder-based frustration models could provide additional insight. Although the idea that disorder could promote order is counter-intuitive, it has been shown in the past that site and/or bond defects in a magnetically ordered lattice may, in some particular conditions, give rise to a spiral³⁵⁻³⁶. If a disorder-based mechanism is at the origin of the spiral in YBaCuFeO₅, the most affected coupling will probably be the intra-bowtie coupling J_{c2} because both, its sign and its magnitude are strongly dependent of which cations occupy the bowties (Cu-Fe: FM, Fe-Fe: AFM, Cu-Cu: negligible small). Interestingly, it is found experimentally that the deviation from collinearity by entering the spiral phase occurs *exclusively* within the bipyramidal units (Figs. 1b and c).

As mentioned in introduction, the bowties are expected to be occupied by FM Cu-Fe pairs²¹. On the other hand, we show in Figs. 3c and 3d that the size of the pyramids (d_2) changes with the degree of average disorder, suggesting that the “Cu-Fe occupation” rule may not be always fulfilled. Based on the results of DFT calculations we don’t expect a lot of Fe-Fe/Cu-Cu defects (as shown in ref.²¹, Cu/Fe distributions with Fe-Fe and/or Cu-Cu pairs in the bipyramids are more expensive). However, we cannot exclude having small, cooling-rate dependent amounts. Interestingly, Fe-Fe defects are strongly AFM (about 100 times larger in absolute value than the FM Cu-Fe coupling). Hence, a few of them could produce important perturbations the in underlying collinear magnetic order. Establishing whether they may turn the collinear order into a spiral is out of the scope of this work and will need further investigation.

To summarize, we have shown that Cu-Fe chemical disorder plays a prominent role in the control of the temperature stability range of the two ordered magnetic phases present in YBaCuFeO₅. Although disorder changes very little the energy scale responsible for the paramagnetic-to-collinear AFM transition at T_{N1} , it dramatically increases the degree of frustration and the related collinear-to-spiral transition at T_{N2} . As a result, the stability range of the spiral phase is extended by more than 150K and its upper limit pushed beyond RT at zero magnetic field. Our findings show that this novel mechanism can be effectively used to engineer the properties of a magnetic spiral, including its wavelength, orientation and stability range. Although our samples are too leaky to sustain electric polarization at RT (Supplementary Table 1), these results may be relevant for the design of other spiral magnets with magnetoelectric properties beyond room temperature.

Methods

Synthesis

The YBaCuFeO₅ ceramic samples were prepared by solid state synthesis. High purity (Aldrich, 99.999% trace metals basis) stoichiometric amounts of BaCO₃, Y₂O₃, CuO and Fe₂O₃ were used to prepare 40g of starting material. After a pre-annealing of Y₂O₃ oxide at 900°C for 10h the starting oxides were thoroughly mixed and fired at 1150°C for 50h under oxygen gas flow. The obtained black powder was grounded again and divided into 5 identical portions that were pelletized, separately sintered at 1150°C for 50h in air and cooled to RT in different conditions. We used 5, 100, 300 and 500 K h⁻¹ for four of the samples, whereas the fifth one was quenched into liquid

nitrogen. The phase purity was checked by laboratory x-ray powder diffraction (Bruker D8 Advance, Cu $K\alpha$), which indicated the absence of impurity phases and an excellent crystallinity. The oxygen content, as determined from thermogravimetric H_2 -reduction, was very close to the sample formula. All samples showed deviations from the nominal stoichiometry smaller than 1%, in agreement with the results of the Rietveld analysis.

Magnetic susceptibility

DC magnetization measurements were carried out on a superconducting quantum interference device magnetometer (MPMS XL, Quantum Design) equipped with oven. YBaCuFeO₅ pellets ($m \sim 20\text{mg}$, $D \sim 3\text{ mm}$, $H \sim 1\text{ mm}$) from the same batches as the samples used for the neutron and x-ray diffraction measurements were mounted in transparent drinking straws and cooled in zero field down to 1.8K. The magnetization M of the sample was then measured in a magnetic field $B = \mu_0 H = 0.5\text{ T}$ up to 400K by heating. For the high temperature measurements (300-500K) the samples were wrapped in Al foil as described in ref.³⁷. After application of a magnetic field of 0.5 T the magnetization was measured by heating. The signal from the empty sample holders was separately measured in the same conditions and subtracted from the data. The magnetic susceptibility $\chi^{\text{DC}} = M/B$ was then calculated for all samples. The values of T_{N1} and T_{N2} mentioned in the text correspond to the maxima of the χ^{DC} vs temperature curves.

Neutron and synchrotron x-ray diffraction

Neutron powder diffraction (NPD) measurements were carried out at the Swiss Neutron Source SINQ of the Paul Scherrer Institute in Villigen, Switzerland. The

samples were introduced in cylindrical vanadium sample cans ($D = 0.6$ cm, $H = 5$ cm) and mounted on the stick of a cryofurnace. Neutron diffraction patterns were continuously recorded at the powder diffractometer DMC³⁸⁻³⁹ (Pyrolitic Graphite (002), $2\theta_{\max} = 104^\circ$, $2\theta_{\text{step}} = 0.1^\circ$, $\lambda = 4.5$ Å) while ramping the temperature from 1.5 to 500 K. Longer acquisitions for magnetic structure refinements were made at 10K and RT with $2\theta_{\max} = 130^\circ$. High resolution patterns at these two temperatures were also recorded at the powder diffractometer HRPT⁴⁰ (Ge (822), $2\theta_{\max} = 160^\circ$, $2\theta_{\text{step}} = 0.05^\circ$, $\lambda = 1.1546$ Å). In both instruments the background from the sample environment was minimized using oscillating radial collimators. The wavelengths and zero offsets were determined using a NAC reference powder sample. The values of T_{N1} and T_{N2} , defined respectively as the setup and the maximum of the $(\frac{1}{2} \frac{1}{2} \frac{1}{2})$ magnetic Bragg reflection, were found to coincide with maxima of the χ^{DC} vs temperature curves (Supplementary Fig. 1).

Synchrotron x-ray powder diffraction (SXRPD) measurements were performed at the Swiss Light Source (SLS) of the Paul Scherrer Institute in Villigen, Switzerland. All samples were loaded in borosilicate glass capillaries ($D = 0.1$ mm, $\mu R = 0.53$) and measured at RT in transmission mode with a rotational speed of ~ 2 Hz at the Materials Science Beamline⁴¹ (Si (111), $\lambda = 0.77627$ Å). The primary beam was vertically focused and slitted to about 300×4000 μm^2 . Powder diffraction patterns were recorded at eight different detector positions for 10 s at RT using a Mythen II 1D multistrip detector (Dectris) with energy discrimination ($2\theta_{\max} = 120^\circ$, $2\theta_{\text{step}} = 0.0036^\circ$, threshold at 12000 eV) and then binned into one pattern. The wavelength and zero offset were determined using a Si reference powder sample (NIST SRM 640d).

Data analysis

All diffraction data were analyzed using the Rietveld package FullProf Suite⁴²⁻⁴³. The structural and magnetic refinements were carried out by combining the data sets recorded at the same temperature: RT (HRPT + MSBL, Supplementary Figure 2); 10K (HRPT + DMC, Supplementary Figure 1). We used the non-centrosymmetric space group P4mm for the description of the crystal structure, which enables to refine separately the z coordinates and the occupation of the split Cu and Fe sites. Anisotropic Debye-Waller factors were used for all atoms with exception of Cu and Fe. The z coordinates of the two basal oxygen sites O2 and O2' were refined separately but their MSD restricted to have the same value (Supplementary Table 1). The possible existence of extra oxygen in the Y layers was checked by introducing a new O site at the position ($\frac{1}{2}, \frac{1}{2}, z$) with $z \sim 0.5$. Attempts to refine the z coordinate and the site occupancy led to unstable fits, indicating that extra oxygen, if any, is below the detection limit of neutron powder diffraction.

The collinear and spiral magnetic structures were described according to the models reported in ref.⁴⁴. The ratio between the Fe and Cu magnetic moments was restricted to have the same ratio than their free ion, spin-only values (5:1). Below T_{N2} , where the collinear and spiral phases coexist (Supplementary Figure 1 and Supplementary Table 1), the Fe and Cu magnetic moments were restricted to have the same value and the same inclination with respect to the **ab** plane in the two magnetic phases.

Data availability

Data supporting the finding of this study are available from the corresponding author upon reasonable request.

Code availability

FullProf Suite is available free of charge at <https://www.ill.eu/sites/fullprof/>

REFERENCES

1. Herpin A., *Théorie du magnétisme*, Presses Universitaires de France, Paris (1968).
2. Goodenough, J. B. *Magnetism and the Chemical Bond*; Wiley, Cambridge, MA, (1963).
3. Shimizu, T., Matsumoto, T., Goto, A., Chandrasekhar Rao, T.V., Yoshimura, K. and Kosuge, K. Spin susceptibility and superexchange interaction in the antiferromagnet CuO. *Phys. Rev. B* **68**, 224433-224440 (2003).
4. Giovanetti, G., Kumar, S., Stroppa, A., van den Brink, J., Picozzi, S. and Lorenzana, J. High- T_C ferroelectricity emerging from magnetic degeneracy in cupric oxide. *Phys. Rev. Lett.* **106**, 026401-026405 (2011).
5. Forsyth, J.B., Brown, P.J. and Wanklyn B.M. Magnetism in cupric oxide. *J. Phys. C: Solid State Phys.* **21**, 2917-2929 (1988).
6. Hellsvik J., Balestieri M., Usui T., Stroppa A., Bergman A., Bergqvist L., Prabhakaran D., Eriksson O., Picozzi S., Kimura T. and Lorenzana J. Tuning order-by-disorder multiferroicity in CuO by doping. *Phys. Rev. B* **90**, 014437-014445 (2014).

7. Rocquefelte, X., Schwarz K., Blaha P., Kumar S. and van den Brink J. Room-temperature spin-spiral multiferroicity in high-pressure cupric oxide. *Nature Communications* **4**:2511 (2013).
8. Kimura T, Goto T, Shintani H, Ishizaka K, Arima T and Tokura Y. Magnetic control of ferroelectric polarization. *Nature* **426**, 55–8 (2003).
9. Kenzelmann M., Harris A.B., Jonas S., Broholm C., Schefer J., Kim S.B., Zhang C.L., Cheong S.-W., Vajk O.P., Lynn J.W. Magnetic inversion symmetry breaking and ferroelectricity in TbMnO₃. *Phys. Rev. Lett.* **95**, 087206 (2005).
10. Arkenbout A., Palstra T., Siegrist T. and Kimura T. Ferroelectricity in the cycloidal spiral magnetic phase of MnWO₄. *Phys. Rev. B* **74**, 184431-184438 (2006).
11. Naito Y., Sato K., Yasui Y., Kobayashi Y. and Sato M. Ferroelectric transition induced by the incommensurate magnetic ordering in LiCuVO₄. *J. Phys. Soc. Japan* **76**, 023708-023713 (2007).
12. Seki S., Kurumaji T., Ishiwata S., Matsui H., Murakawa H., Tokunaga Y., Kaneko Y., Hasegawa T. and Tokura Y. Cupric chloride CuCl₂ as an S= 1 chain multiferroic. *Phys. Rev. B* **82** 064424-064428 (2010).
13. Bibes, M. and Barthelemy, A. Multiferroics: Towards a magnetoelectric memory. *Nat. Mater.* **7**, 425-426 (2008).
14. Scott, J. F. Room-temperature multiferroic magnetoelectrics. *NPG Asia Mater.* **5**, e72 (2013).
15. Spaldin, N.A. & Fiebig M. The renaissance of magnetoelectric multiferroics. *Science* **309**, 391-392 (2005).

16. Katsura, H., Nagaosa, N. & Balatsky, A. V. Spin current and magnetoelectric effect in noncollinear magnets. *Phys. Rev. Lett.* **95**, 057205 (2005).
17. Mostovoy, M. Ferroelectricity in spiral magnets. *Phys. Rev. Lett.* **96**, 067601 (2006).
18. Arima, T. Ferroelectricity induced by proper-screw type magnetic order. *J. Phys. Soc. Japan* **76**, 073702 (2007).
19. Tokura Y, Seki S and Nagaosa N. Multiferroics of spin origin. *Rep. Prog. Phys.* **77**, 076501-076546 (2014).
20. Kimura Y. Magnetoelectric hexaferrites. *Annu. Rev. Condens. Matter Phys.* **3**, 93-110 (2012).
21. Morin M., Scaramucci A., Bartkowiak M., Pomjakushina E., Deng G., Sheptyakov D., Keller L., Rodriguez-Carvajal J., Spaldin N.A., Kenzelmann M., Conder K., and Medarde M. Incommensurate magnetic structure, Fe/Cu chemical disorder, and magnetic interactions in the high-temperature multiferroic YBaCuFeO₅ *Phys. Rev. B* **91**, 064408-064421 (2015).
22. Kimura T., Sekio Y., Nakamura H., Siegrist T. and Ramirez A. Cupric oxide as induced-multiferroic with high T_c. *Nature Mater.* **7**, 291-294 (2008).
23. Kundys B., Maignan A. and Simon C. Multiferroicity with high-T_c in ceramics of the YBaCuFeO₅ ordered perovskite. *Appl. Phys. Lett.* **94**, 072506-072508 (2009).
24. Kawamura Y., Kai T., Satomi E., Yasui Y., Kobayashi Y., Sato M., and Kakurai K. High-Temperature Multiferroic State of RBaCuFeO₅ (R = Y, Lu, and Tm). *J. Phys. Soc. Jpn.* **79**, 073705-073708 (2010).

25. Caignaert V., Mirabeau I., Bourée F., Nguyen N., Ducouret A., Greneche J.-M., and Raveau B. Crystal and magnetic structure of YBaCuFeO₅. *J. Solid State Chem.* **114**, 24-35 (1995).
26. Mombrú A.W. Prassides K., Christides C., Erwik R., Pissas M., Mitros C. and Niarchos D. Neutron powder diffraction study (T = 4.2-300 K) and polarization analysis of YBaCuFeO_{5+d}. *J. Phys.: Condens. Matter* **10**, 1247-1258 (1998).
27. Ruiz-Aragon M.J., Amador U., Martinez J.L., Andersen N.H. and Ehrenberg H. Low-temperature magnetic structure of YBaCuFeO₅ and the effect of partial substitution of yttrium by calcium. *Phys. Rev. B* **58**, 6291-6297 (1998).
28. Klyndyuk A.I., Petrov G.S. and Bashirov I.A. Phase transformations of YBaCuFeO₅ at 460 and 560K. *Inorg. Mater* **35**, 954-956 (1999).
29. Goodenough J.B. An interpretation of the magnetic properties of the perovskite-type mixed crystals La_{1-x}Sr_xCoO_{3-λ}. *J. Phys. Chem. Solids* **6**, 287-297 (1958).
30. Kanamori J. Superexchange interaction and symmetry properties of solids. *J. Phys. Chem. Solids* **10**, 87-98 (1959).
31. Anderson P.W. New approach to the theory of superexchange interactions. *Phys. Rev.* **115**, 2-13 (1959).
32. Medarde M., Mitchell J.F., Millburn J.E., Short S and Jorgensen J.D. Optimal T_C in layered manganites: different roles of coherent and incoherent lattice distortions. *Phys. Rev. Lett.* **83**, 1223-1226 (1999).

33. Grundmann H., Schilling A., Medarde M. and Sheptyakov D. Influence of disorder on the structural phase transition and magnetic interactions in $\text{Ba}_{3-x}\text{Sr}_x\text{Cr}_2\text{O}_8$. *Phys. Rev. B* **90**, 075101-075107 (2014).
34. Hida, K. Ground-state phase diagram of the spin-1/2 ferromagnetic-antiferromagnetic alternating Heisenberg chain with anisotropy. *Phys. Rev. B* **46**, 8268 (1992)
35. Schraiman, I. and Siggia, E.D., Spiral phase of a doped quantum antiferromagnet. *Phys. Rev. Lett.* **62**, 1564 (1989).
36. Ivanov N.B., Krüger, S.E. and Richter J., Square-Lattice Heisenberg antiferromagnet with two kinds of nearest-neighbor bonds. *Phys. Rev. B.* **53**, 2633 (1996).
37. Sesé J., BartolomeJ. and Rillo C., Disposable sample holder for high temperature measurements in MPMS superconducting quantum interference device magnetometers, *Rev. Sci. Instrum.* **78**, 046101-046103 (2007).
38. Schefer J., Fischer P., Heer H., Isacson A., Koch M., and Thut R. A versatile double-axis multiscan neutron powder diffractometer, *Nucl. Instr. and Meth. A* **288**, 477-485 (1990).
39. Fischer P., Keller L., Schefer J. and Kohlbrecher J., Neutron diffraction at SINQ, *Neutron News* **11** No.3 19-21 (2000).
40. Fischer P., Frey G. , Koch M., Könnecke M., Pomjakushin V., Schefer J., Thut R., Schlumpf N., Bürge R., Greuter U., Bondt D. and Berruyer E., High-resolution

powder diffractometer HRPT for thermal neutrons at SINQ, *Physica B* **146**, 276-278 (2000).

41. Willmott P.R., Meister D., Leake S.J., Lange M., Bergamaschi A., Böge M., Calvi M., Cancellieri C., Casati N., Cervellino A., Chen Q., David C., Flechsig U., Gozzo F., Henrich B., Jäggi-Spielmann S., Jakob B., Kalichava I., Karvinen P., Krempasky J., Lüdeke A., Lüscher R., Maag S., Quitmann C., Reinle-Schmitt M.L., Schmidt T., Schmitt B., Streun A., Vartiainen I., Vitins I., Wanga X. and Wulschlegera R. The Materials Science beamline upgrade at the Swiss Light Source, *J. Synchrotron Rad.* **20**, 667–682 (2013).

42. Rodríguez-Carvajal J., Recent advances in magnetic structure determination by neutron powder diffraction + FullProf, *Physica B* **192**, 55-56 (1993).

43. Rodríguez-Carvajal J., Recent developments of the program FullProf, *Commission of powder diffraction (IUCR), Newsletter No.* **26**, 12-19 (2001).

Acknowledgements

We thank A. Scaramucci, N. Spaldin, M. Müller, C. Mudry, T. Shang, R. Frison and H-B. Bürgi for fruitful discussions. This work was supported by the Swiss National Science Foundation (Grant No. 200021-141334) and the European Community's 7th Framework Program (Grant No. 290605; COFUND: PSI-FELLOW). We acknowledge the allocation of beam time at the Swiss Neutron Source SINQ (HRPT and DMC diffractometers) and the Swiss Light Source SLS (Materials Science Beam Line).

Author contributions

Mi.M. and Ma.M. conceived and led the project, Mi.M., A.R., K.C. and E.P. synthesized the samples, Mi.M., Ma.M., A.R., E.C. and D.S. performed the neutron diffraction measurements, Mi.M. and V.B. carried out the synchrotron x-ray diffraction experiments, Mi.M., A.R. and M.B. measured the magnetic susceptibility, Mi.M., Ma.M., A.R. and E.C. analyzed all the experimental data. Ma.M., Mi.K. and Mi.M wrote the paper with the input from all authors.

Competing financial interests

The authors declare no competing financial interests.

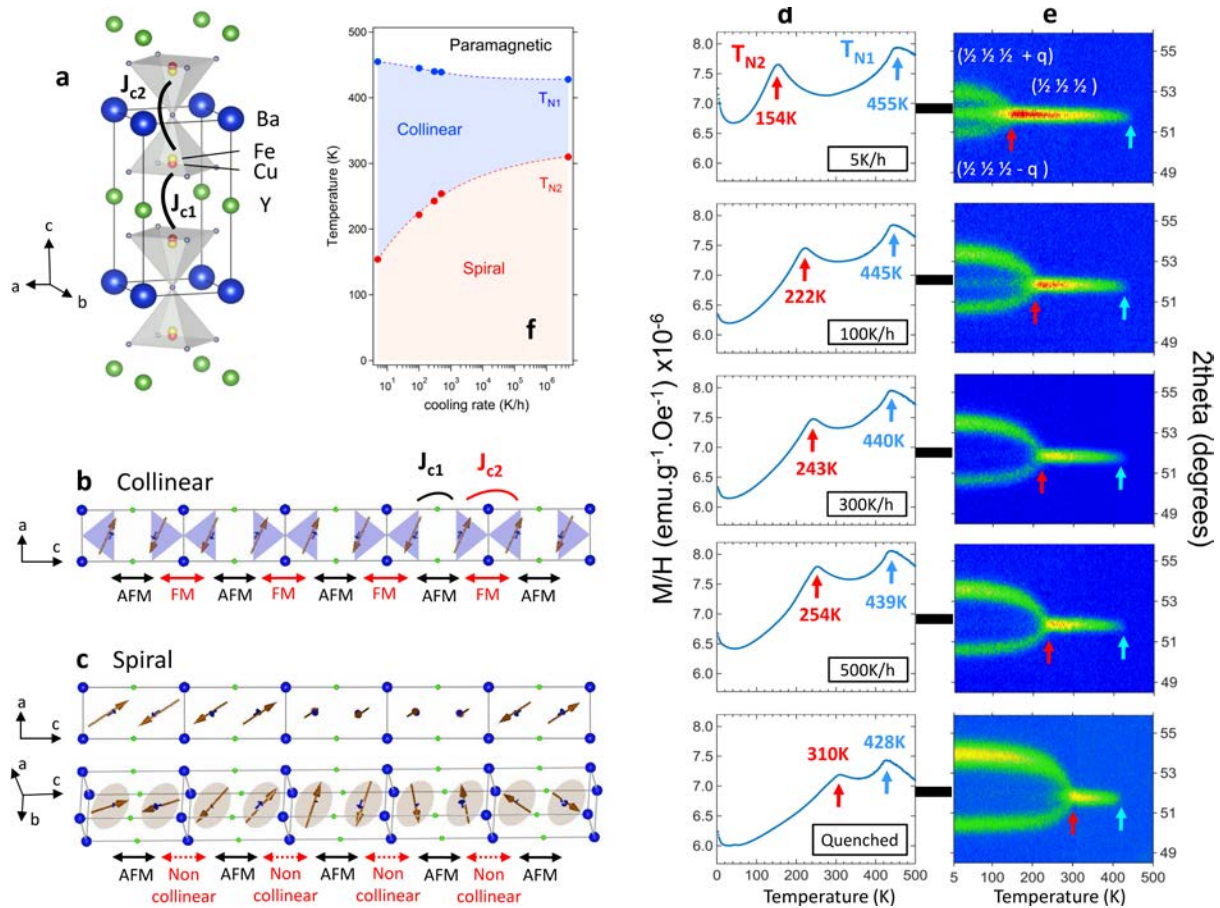


Figure 1: Dependence of the magnetic transition temperatures T_{N1} and T_{N2} with the cooling rate. **a**, Crystal structure of YBaCuFeO₅ showing the Cu/Fe disorder in the bipyramidal sites. **b,c**, Magnetic structures in the commensurate collinear (**b**) and incommensurate spiral phases (**c**). In both cases, only $\frac{1}{4}$ of the magnetic unit cell is shown. The rotation plane of the spiral is indicated for clarity. The NN magnetic couplings along the **c** crystal axis are also shown. **d**, Mass magnetic susceptibility M/H as a function of temperature measured under the application of an external magnetic field of 5000 Oe for the five YBaCuFeO₅ powder samples prepared using different cooling rates in the last annealing. **e**, Contour maps showing the temperature dependence of the position and the intensities of the magnetic Bragg reflection $(\frac{1}{2} \frac{1}{2} \frac{1}{2})$ associated to the high temperature collinear antiferromagnetic phase, and the $(\frac{1}{2} \frac{1}{2} \frac{1}{2} \pm q)$ satellites of the low temperature

magnetic spiral phase for the five samples. The measurements were performed by heating at the neutron powder diffractometer DMC (SINQ, Switzerland) using a wavelength $\lambda = 4.5 \text{ \AA}$. The blue and red arrows indicate respectively the magnetic transition temperatures T_{N1} and T_{N2} . **f**, Stability range of the collinear and spiral phases with the cooling rate. Dashed lines are guide for the eye.

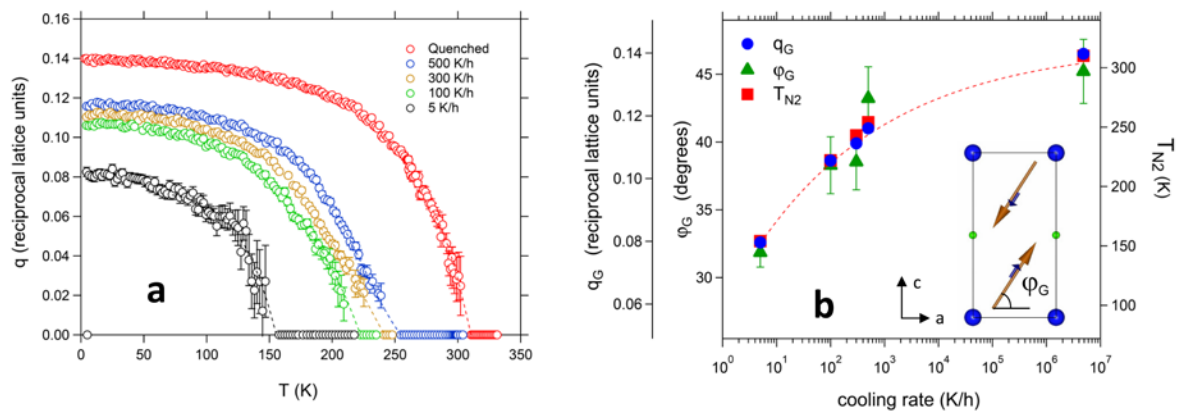


Figure 2: Changes in the spiral magnetic order with the cooling rate. a, Temperature dependence of the modulus of the magnetic modulation vector q for the five YBaCuFeO_5 samples. For each sample, q has been set to zero for $T > T_{N2}$. The dashed lines are guides for the eye. **b**, Evolution of the collinear-to-spiral transition temperature (T_{N2}) and the ground state values ($T = 10\text{K}$) of the modulus of the magnetic modulation vector (q_G) and the inclination of the spiral rotation plane (φ_G). The figure shows the positive correlation between the three quantities and the cooling rate. The error bars of q_G and T_{N2} are smaller than the size of the symbols and the dotted line is a guide for the eye. The inclination angle φ is the complementary of the angle $\theta = 90 - \varphi$ used in ref.²¹. The error bars of q and φ_G are the standard deviations obtained from the fits of the magnetic structure using the FullProf Suite Rietveld package⁴¹⁻⁴².

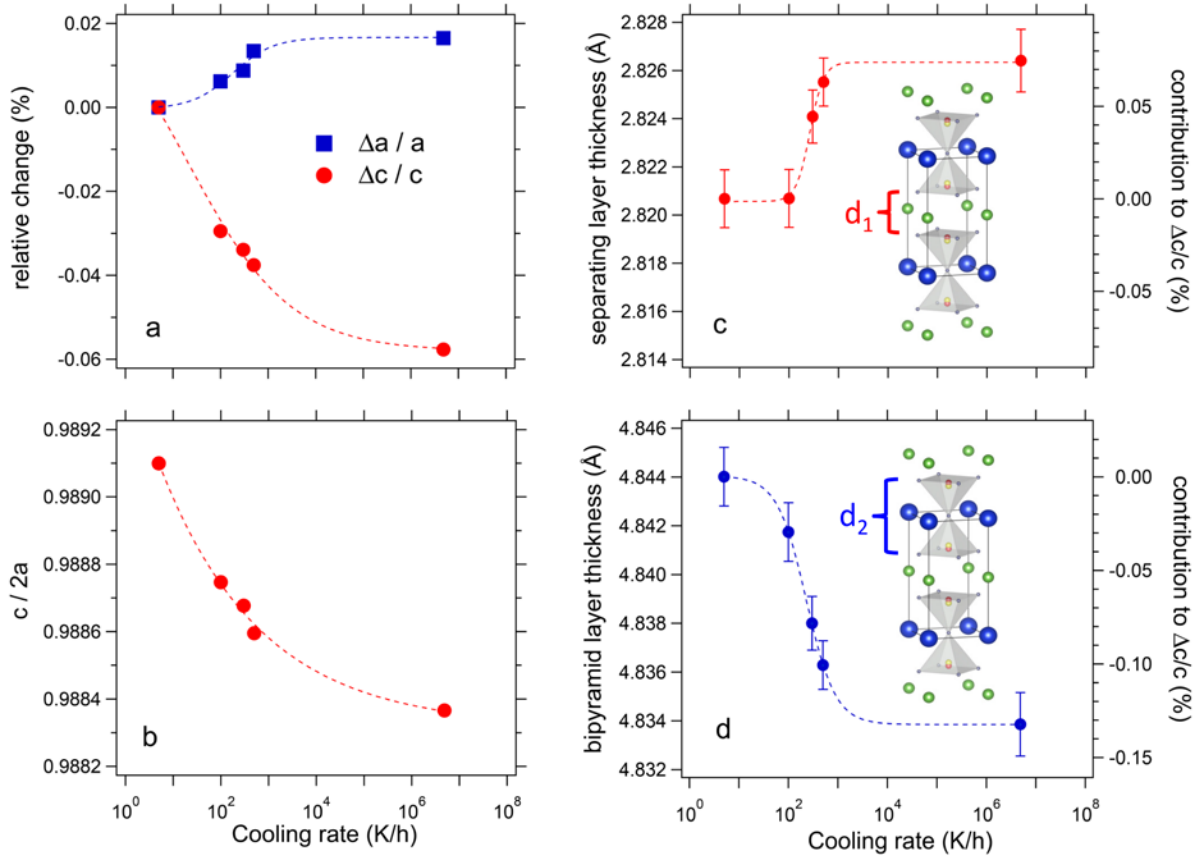


Figure 3: Changes in the RT crystal structure with cooling rate. **a**, Relative change (%) of the lattice parameters a and c with respect to those of the sample with the lowest T_{N2} . **b**, Tensile ($c/2a < 1$) tetragonal distortion. **c**, Thickness of the Y-containing separating layers (d_1). **d**, Thickness of the bipyramid layers (d_2). The right vertical axis in **c** and **d** indicates the percent contribution of d_1 and d_2 to the variation of the c axis with the cooling rate. Dashed lines are guides for the eye. All values were extracted from the combined (neutron and x-ray synchrotron) Rietveld fits of the powder diffraction data at RT. The error bars of the lattice parameters and the interatomic distances are the standard deviations obtained from the fits of the crystal structure using the FullProf Suite Rietveld package⁴¹⁻⁴². In the case of **a** and **b**, they are smaller than the marker size.

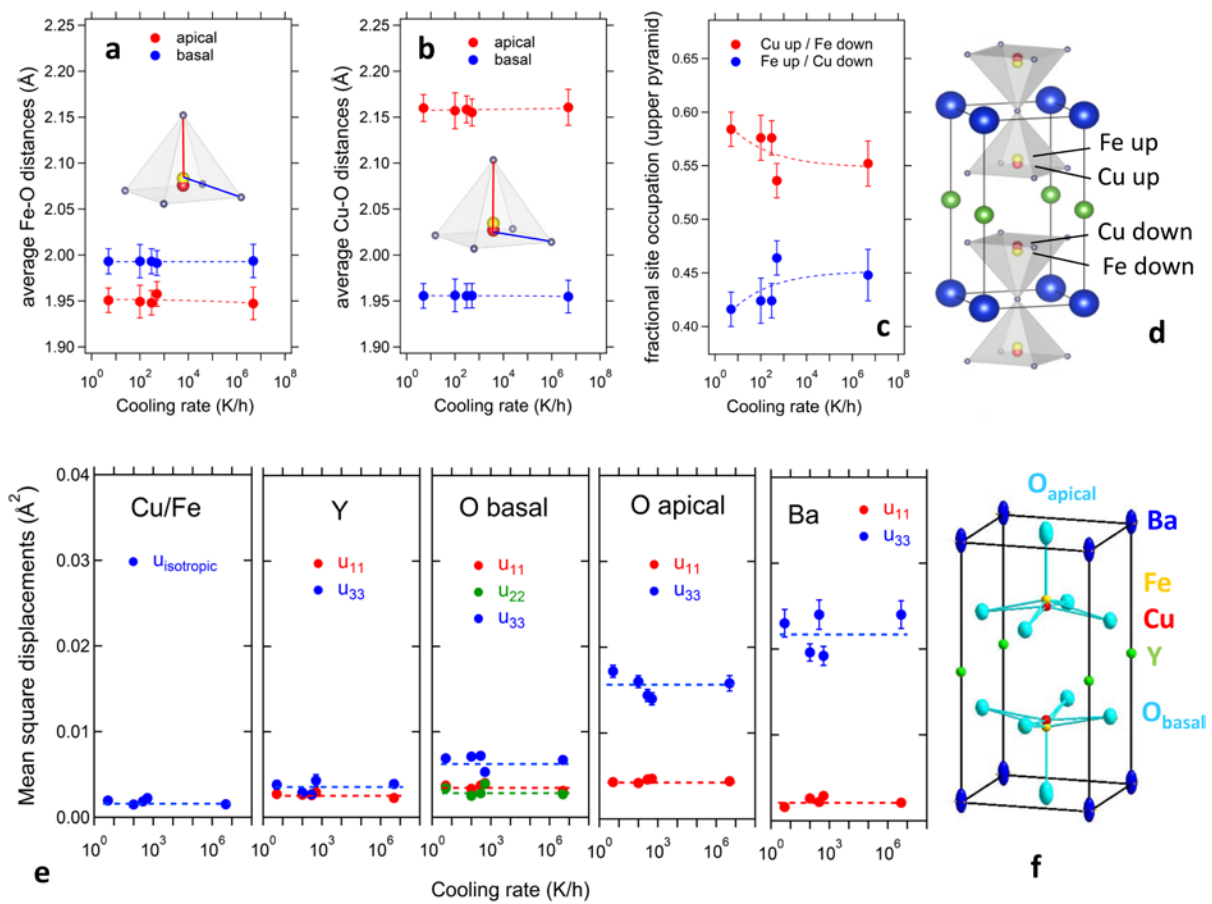


Figure 4: Evolution of the average Cu/Fe chemical disorder with the cooling rate. a,b Fe-O and Cu-O interatomic distances at RT. **c-d**, Cu/Fe occupation of the split B-sites in the pyramids, as obtained from the combined neutron and x-ray synchrotron Rietveld fits at RT. **e**, Anisotropic mean-square displacements of all atomic sites at 10K. **f**, Thermal ellipsoids (90% probability) at RT. Dashed lines are guides for the eye. The error bars of the interatomic distances, the Cu/Fe occupation and the MSD's are the standard deviations obtained from the fits of the crystal structure using the FullProf Suite Rietveld package⁴²⁻⁴³.